Evanescent waves in high numerical aperture aplanatic solid immersion microscopy: Effects of forbidden light on subsurface imaging

Abdulkadir Yurt,[1,5] Aydan Uyar,[2,5] T. Berkin Cilingiroglu,[2] Bennett B. Goldberg,[2,3,4,6] and M. Selim Ünlü[2,3,4,*]

[1] *Division of Materials Science and Engineering, Boston University, Brookline, Massachusetts, USA*
[2] *Department of Electrical and Computer Engineering, Boston University, Boston, Massachusetts, USA*
[3] *Department of Biomedical Engineering, Boston University, Boston, Massachusetts, USA*
[4] *Department of Physics, Boston University, Boston, Massachusetts, USA*
[5] *These authors contributed equally to this work.*
[6] *goldberg@bu.edu*
[*] *selim@bu.edu*

Abstract: The collection of light at very high numerical aperture allows detection of evanescent waves above the critical angle of total internal reflection in solid immersion lens microscopy. We investigate the effect of such evanescent modes, so-called forbidden light, on the far-field imaging properties of an aplanatic solid immersion microscope by developing a dyadic Green's function formalism in the context of subsurface semiconductor integrated circuit imaging. We demonstrate that the collection of forbidden light allows for sub-diffraction spatial resolution and substantial enhancement of photon collection efficiency albeit inducing wave-front discontinuities and aberrations.

OCIS codes: (110.0180) Microscopy; (110.1758) Computational imaging.

References and links

1. S. Bianic, A. Allemand, G. Kerrosa, P. Scafidi, and D. Renard, "Advanced backside failure analysis in 65nm CMOS technology," Microelectron. Reliab. **47**(9-11), 1550–1554 (2007).
2. Y. Zhang, "Design of high-performance supersphere solid immersion lenses," Appl. Opt. **45**(19), 4540–4546 (2006).
3. S. H. Goh, C. J. R. Sheppard, A. C. T. Quah, C. M. Chua, L. S. Koh, and J. C. H. Phang, "Design considerations for refractive solid immersion lens: Application to subsurface integrated circuit fault localization using laser induced techniques," Rev. Sci. Instrum. **80**(1), 013703 (2009).
4. E. Ramsay, K. A. Serrels, M. J. Thomson, A. J. Waddie, M. R. Taghizadeh, R. J. Warburton, and D. T. Reid, "Three-dimensional nanoscale subsurface optical imaging of silicon circuits," Appl. Phys. Lett. **90**(13), 131101 (2007).
5. F. H. Köklü, S. B. Ippolito, B. B. Goldberg, and M. S. Ünlü, "Subsurface microscopy of integrated circuits with angular spectrum and polarization control," Opt. Lett. **34**(8), 1261–1263 (2009).
6. K. A. Serrels, E. Ramsay, R. J. Warburton, and D. T. Reid, "Nanoscale optical microscopy in the vectorial focusing regime," Nature Pho. **2**(5), 311–314 (2008).
7. A. Yurt, E. Ramsay, F. H. Köklü, C. R. Stockbridge, Y. Lu, M. S. Ünlü, and B. B. Goldberg, "Dual-Phase Interferometric Confocal Imaging for Electrical Signal Modulation Mapping in ICs," in *Proc. of the 38th International Symposium for Testing and Failure Analysis* (ASM International, 2012), 172–175 (2012).
8. W. Lukosz and R. E. Kunz, "Light emission by magnetic and electric dipoles close to a plane interface. I. Total radiated power," J. Opt. Soc. Am. **67**(12), 1607–1615 (1977).
9. L. Novotny, "Allowed and forbidden light in near-field optics. I. A single dipolar light source," J. Opt. Soc. Am. A **14**(1), 91–104 (1997).
10. J. Enderlein and M. Böhmer, "Influence of interface-dipole interactions on the efficiency of fluorescence light collection near surfaces," Opt. Lett. **28**(11), 941–943 (2003).
11. S. B. Ippolito, S. A. Thorne, M. G. Eraslan, B. B. Goldberg, M. S. Ünlü, and Y. Leblebici, "High spatial resolution subsurface thermal emission microscopy," Appl. Phys. Lett. **84**(22), 4529–4531 (2004).
12. F. H. Köklü, J. I. Quesnel, A. N. Vamivakas, S. B. Ippolito, B. B. Goldberg, and M. S. Unlü, "Widefield subsurface microscopy of integrated circuits," Opt. Express **16**(13), 9501–9506 (2008).
13. S. B. Ippolito, B. B. Goldberg, and M. S. Ünlü, "Theoretical analysis of numerical aperture increasing lens microscopy," J. Appl. Phys. **97**(5), 053105 (2005).

#204581 - $15.00 USD Received 27 Jan 2014; revised 10 Mar 2014; accepted 11 Mar 2014; published 24 Mar 2014

14. R. Chen, K. Agarwal, Y. Zhong, C. J. R. Sheppard, J. C. H. Phang, and X. D. Chen, “Complete modeling of subsurface microscopy system based on aplanatic solid immersion lens,” J. Opt. Soc. Am. A **29**(11), 2350–2359 (2012).
15. R. Chen, K. Agarwal, C. J. R. Sheppard, J. C. H. Phang, and X. Chen, “A complete and computationally efficient numerical model of aplanatic solid immersion lens scanning microscope,” Opt. Express **21**(12), 14316–14330 (2013).
16. L. Hu, R. Chen, K. Agarwal, C. J. R. Sheppard, J. C. H. Phang, and X. Chen, “Dyadic Green’s function for aplanatic solid immersion lens based sub-surface microscopy,” Opt. Express **19**(20), 19280–19295 (2011).
17. Throughout the article, the term “sub-diffraction” refers to a length scale smaller than the fundamental diffraction limit according to Rayleigh’s definition (0.61λ where the λ is the wavelength of light in the medium).
18. A. N. Vamivakas, M. Atatüre, J. Dreiser, S. T. Yilmaz, A. Badolato, A. K. Swan, B. B. Goldberg, A. Imamoglu, and M. S. Ünlü, “Strong Extinction of a Far-Field Laser Beam by a Single Quantum Dot,” Nano Lett. **7**(9), 2892–2896 (2007).
19. L. Wang, M. C. Pitter, and M. G. Somekh, “Wide-field high-resolution structured illumination solid immersion fluorescence microscopy,” Opt. Lett. **36**(15), 2794–2796 (2011).
20. K. Karrai, X. Lorenz, and L. Novotny, “Enhanced reflectivity contrast in confocal solid immersion lens microscopy,” Appl. Phys. Lett. **77**(21), 3459–3461 (2000).
21. M. Lang, E. Aspnes, and T. D. Milster, “Geometrical analysis of third-order aberrations for a solid immersion lens,” Opt. Express **16**(24), 20008–20028 (2008).
22. Y. Lu, T. Bifano, S. Ünlü, and B. Goldberg, “Aberration compensation in aplanatic solid immersion lens microscopy,” Opt. Express **21**(23), 28189–28197 (2013).
23. L. Novotny and B. Hecht, *Principles of Nano-Optics* (Cambridge U. Press, 2006).
24. M. B. Pereira, J. S. Craven, and S. B. Mendes, “Solid immersion lens at the aplanatic condition for enhancing the spectral bandwidth of a waveguide grating coupler,” Opt. Eng. **49**(12), 124601 (2010).
25. B. B. Goldberg, A. Yurt, Y. Lu, E. Ramsay, F. H. Köklü, J. Mertz, T. G. Bifano, and M. S. Ünlü, “Chromatic and spherical aberration correction for silicon aplanatic solid immersion lens for fault isolation and photon emission microscopy of integrated circuits,” Microelectron. Reliab. **51**(9-11), 1637–1639 (2011).
26. K. A. Serrels, E. Ramsay, P. A. Dalgarno, B. Gerardot, J. O’Connor, R. H. Hadfield, R. J. Warburton, and D. T. Reid, “Solid immersion lens applications for nanophotonic devices,” J. Nanophoton. **2**(1), 021854 (2008).
27. C. Liu and S. H. Park, “Numerical analysis of an annular-aperture solid immersion lens,” Opt. Lett. **29**(15), 1742–1744 (2004).
28. D. R. Mason, M. V. Jouravlev, and K. S. Kim, “Enhanced resolution beyond the Abbe diffraction limit with wavelength-scale solid immersion lenses,” Opt. Lett. **35**(12), 2007–2009 (2010).
29. J. Enderlein, I. Gregor, and T. Ruckstuhl, “Imaging properties of supercritical angle fluorescence optics,” Opt. Express **19**(9), 8011–8018 (2011).
30. Note that the circularly asymmetric intensity distribution in the allowed zone is obscured due to the logarithmic scale and the range on the plots.
31. O. Haeberlé, M. Ammar, H. Furukawa, K. Tenjimbayashi, and P. Török, “The point spread function of optical microscopes imaging through stratified media,” Opt. Express **11**(22), 2964–2969 (2003).
32. P. Török, “Propagation of electromagnetic dipole waves through dielectric interfaces,” Opt. Lett. **25**(19), 1463–1465 (2000).
33. F. Goos and H. Hänchen, “Ein neuer und fundamentaler Versuch zur Totalreflexion,” Ann. Phys. **436**(7-8), 333–346 (1947).
34. A. J. den Dekker and A. van den Bos, “Resolution: a survey,” J. Opt. Soc. Am. A **14**(3), 547–557 (1997).
35. C. M. Sparrow, “On spectroscopic resolving power,” Astrophys. J. **44**, 76–86 (1916).
36. T. Asakura, “Resolution of two unequally bright points with partially coherent light,” Nouv. Rev. Opt. **5**(3), 169–177 (1974).
37. M. Born and E. Wolf, *Principles of Optics* (Cambridge University, 1997).

---

1. Introduction

The growing demand for high spatial resolution in optical inspection for failure analysis of semiconductor integrated circuits (ICs) has aroused interest in employing aplanatic solid immersions lenses (aSILs) [1–7]. In such applications, aSILs are placed in intimate mechanical contact with the polished back-side of an IC chip, hence transforming the silicon substrate into a high refractive index immersion medium (n_{Si} = ~3.5) for high numerical aperture (NA) sub-surface imaging.

The circuit features fabricated on the front-side of the silicon substrate such as resistors, capacitors, interconnects and transistor gates are surrounded by an insulating medium with a lower refractive index (typically, n_{ins} = ~1.5) compared to the silicon immersion index. The electromagnetic boundary conditions at the dielectric interface between the silicon substrate and insulating media impose that the evanescent waves originated from the objects in the insulating medium are transformed into propagating waves in silicon immersion medium at angles higher than the critical angle of total internal reflection (TIR) [8]. Such propagating

#204581 - $15.00 USD Received 27 Jan 2014; revised 10 Mar 2014; accepted 11 Mar 2014; published 24 Mar 2014

waves, so-called forbidden light, can be collected by the aSIL and thus contribute to the far-field imaging [9, 10]. In modern IC manufacturing technology, most important circuit features reside within the depth of the decay length of evanescent waves therefore the forbidden light has important ramifications for high NA imaging of ICs [11, 12]. Recently, the imaging characteristics of aSIL based microscopes have been theoretically investigated [13–16]. Due to their limited scope to imaging objects buried in a homogenous immersion medium, these previous analyses are not directly applicable for assessing the high-NA imaging performance of aSIL through stratified dielectric media such as semiconductor IC chips.

In this article, we investigate the imaging performance of a high-NA aSIL microscope through developing a dyadic Green's function formalism for the analysis of the forbidden light. It is shown that the forbidden light allows sub-diffraction spatial resolution [17] and approximately a factor of 5 improvement in the photon collection efficiency for imaging the metal levels closest to silicon as compared to those at a distance of more than a half-wavelength into the insulating medium. Furthermore, the evanescent nature of the collected light at supercritical angles leads to wave-front aberrations. Investigation of imaging performance in the vicinity of the dielectric interface through an electromagnetic model is critical to assess the limitations of the aSIL microscopy for semiconductor failure analysis and is applicable to imaging in quantum optics [18], biophotonics [19] and metrology [20] as well, as pure ray-tracing models cannot account for the behavior of the evanescent waves discussed here [21, 22].

2. Theory

The theoretical analysis is divided into two steps. We first develop a model of the angular spectrum of the radiation from a dipolar object located in the vicinity of the aplanatic point of the aSIL. Secondly, we present the details of the dyadic Green's function of an aSIL microscope to investigate the high-NA far-field imaging of buried objects beyond the interface between the substrate and the insulating media.

The schematic illustration of the problem is shown in Fig. 1. A dipolar object with an electrical dipole moment $\vec{\mu} = \left(\vec{\mu}_x, \vec{\mu}_y, \vec{\mu}_z\right)$ is located at $\left|\vec{r}_d\right| = \left(x_d, y_d, z_d\right)$ in the insulating medium that has a lower refractive index (n_{ins}) than the silicon immersion medium (n_{aSIL}). The propagating waves in the + z direction of the coordinate system of the microscope undergo refraction at the planar interface between the immersion and insulating media and are channeled towards the subcritical angle cone upon refraction (allowed light, green in Fig. 1). The evanescent waves on the other hand, are transformed into propagating waves beyond the critical angle at the interface (forbidden light, red in Fig. 1). The outward propagating fields in the immersion lens medium comprised of allowed and forbidden light are then refracted on the spherical surface of the aSIL and collected by the backing objective lens. The conventional ray tracing models cannot account such far-field characteristics originating from non-propagating modes and thus an electromagnetic solution is strictly required for the problem. The electromagnetic solution to the problem illustrated in Fig. 1, can be formulated using the Green's function formalism. Assume that the dyadic Green's function $\overleftrightarrow{G}_0(\vec{r},\vec{r}_d)$ defines the electric field $\vec{E}(\vec{r})$ of an electric dipole $\vec{\mu}$ located at $\vec{r}_d$ in the homogenous insulating medium:

$$\vec{E}(\vec{r}) = \omega^2 \mu_0 \overleftrightarrow{G}_0(\vec{r},\vec{r}_d) \cdot \vec{\mu} \tag{1}$$

where ω and μ_0 represent the oscillation frequency of the light and vacuum permeability, respectively. The Green's function satisfying the homogenous space solution is given as [23]:

$$\overset{\leftrightarrow}{\mathrm{G}}_0(\vec{\mathrm{r}}) = \frac{\mathrm{i}}{8\pi^2}\int_{-\infty}^{\infty}\int_{-\infty}^{\infty} \overset{\leftrightarrow}{\mathrm{A}}\, \mathrm{e}^{\mathrm{i}[k_{xins}(x-x_d)+k_{yins}(y-y_d)+k_{zins}(z-z_d)]}\ \mathrm{d}k_{xins}\mathrm{d}k_{yins}$$

$$\overset{\leftrightarrow}{\mathrm{A}} = \frac{1}{k_{ins}^2 k_{zins}}\begin{bmatrix} k_{ins}^2 - k_{xins}^2 & -k_{xins}k_{yins} & -k_{xins}k_{zins} \\ -k_{xins}k_{yins} & k_{ins}^2 - k_{yins}^2 & -k_{yins}k_{zins} \\ -k_{xins}k_{zins} & -k_{yins}k_{zins} & k_{ins}^2 - k_{zins}^2 \end{bmatrix} \tag{2}$$

where k_{ins} refers to the wave-number ($2\pi n_{ins}/\lambda_0$) on which the subscript shows the component in a given coordinate axis. Equation (2) allows us to express the fields of a dipole in Cartesian coordinates in terms of plane and evanescent waves in $z > z_d$ assuming the insulating medium is homogenous. The next step is modifying the Green's function to account for the planar dielectric interface and retain the far-field terms to simplify the solution in Eq. (2) following the procedure in Ref [23]:

$$\overset{\leftrightarrow}{\mathrm{G}}_{\mathrm{aSIL}}(r,\theta_{aSIL},\phi) = \frac{e^{ik_{aSIL}r}}{4\pi r} e^{-i(\vec{k}_{ins}\cdot\vec{r}_d)} e^{i(d(k_{zins}-k_{zaSIL}))}$$

$$\times\begin{bmatrix} 0 & 0 & 0 \\ \cos\phi\cos\theta_{aSIL}\Phi^{(2)} & \sin\phi\cos\theta_{aSIL}\Phi^{(2)} & -\sin\theta_{aSIL}\Phi^{(1)} \\ -\sin\phi\,\Phi^{(3)} & \cos\phi\,\Phi^{(3)} & 0 \end{bmatrix}, \tag{3}$$

$$\Phi^{(1)} = \frac{n_{aSIL}}{n_{ins}}\frac{k_{zaSIL}}{k_{zins}}t_p^{ins},\quad \Phi^{(2)} = \frac{n_{aSIL}}{n_{ins}}t_p^{ins},\quad \Phi^{(3)} = \frac{k_{zaSIL}}{k_{zins}}t_s^{ins}$$

The Green's function in Eq. (3) allows deriving the far-fields in spherical coordinates at a given location in the immersion medium ($r >> \lambda_0$ and $r >> |\vec{\mathrm{r}}_{\mathrm{d}}|$). The terms t_s^{ins} and t_p^{ins} are the Fresnel coefficients for transmission at the planar interface between the immersion and insulating media. The remaining task in the problem is accounting the refraction on the spherical surface of the aSIL in order to find the electric field on the Gaussian reference sphere. Following Ref [16], the electric field on the Gaussian reference sphere is obtained:

$$\vec{\mathrm{E}}^{GRS}(r,\theta_{aSIL},\phi) = \begin{bmatrix} \mathrm{E}_\theta^{\mathrm{GRS}} \\ \mathrm{E}_\phi^{\mathrm{GRS}} \end{bmatrix} = \omega^2\mu_0 \frac{e^{ik_{obj}f_{obj}}}{4\pi f_{obj}} e^{-i(\vec{k}_{ins}\cdot\vec{r}_d)} e^{i(d(k_{zins}-k_{zsil}))}$$

$$\times\begin{bmatrix} \cos\phi\cos\theta_{aSIL}\Phi^{(2)}t_p^{aSIL} & \sin\phi\cos\theta_{aSIL}\Phi^{(2)}t_p^{aSIL} & -\sin\theta_{aSIL}\Phi^{(1)}t_p^{aSIL} \\ -\sin\phi\,\Phi^{(3)}t_s^{aSIL} & \cos\phi\,\Phi^{(3)}t_s^{aSIL} & 0 \end{bmatrix}\cdot\vec{\mu}$$

$$t_p^{aSIL} = \frac{2n_{aSIL}\cos\theta_{obj}}{n_{obj}\cos\theta_{obj} + n_{aSIL}\cos\theta_{aSIL}}\frac{n_{aSIL}}{n_{obj}} \tag{4}$$

$$t_s^{aSIL} = \frac{2n_{aSIL}\cos\theta_{obj}}{n_{aSIL}\cos\theta_{obj} + n_{obj}\cos\theta_{aSIL}}\frac{n_{aSIL}}{n_{obj}}$$

where k_{obj} and k_{ins} are the wave-numbers of the light in the objective and insulating media, respectively; f_{obj} is the focal length of the objective, k_{zins} and k_{zaSIL} are the longitudinal components of the wave-vectors in the insulating and immersion media, respectively; d is the distance of dielectric interface from the aplanatic point; θ_{aSIL} and θ_{obj} represent the polar angles with respect to the aSIL and the objective coordinate centers, respectively.

In a typical aSIL based imaging system, the light collected by the backing objective is focused on a light detector such as a camera by a tube lens. Assuming the aplanatic conditions for objective and the tube lenses, the dyadic Green's function describing the fields on the detector due to an arbitrarily oriented point dipole source near an interface is obtained below:

$$
\begin{aligned}
&\overleftrightarrow{\mathrm{G}}_{\det}(\rho,\varphi,z) = -\frac{ik_{\det} f_{obj}}{8\pi f_{\det}}\sqrt{\frac{n_{obj}}{n_{\det}}}\, e^{i(k_{\det} f_{\det}+k_{obj} f_{obj})}\begin{bmatrix} I_0+I_{21} & I_{22} & -2iI_{11} \\ I_{22} & I_0-I_{21} & -2iI_{12} \\ 0 & 0 & 0 \end{bmatrix}, \\
&I_0 = \int_0^{\theta_{\max}} \sin\theta_{obj}\sqrt{\cos\theta_{obj}}\left(t_s^{aSIL}\Phi^{(3)} + t_p^{aSIL}\Phi^{(2)}\cos\theta_{aSIL}\right)\mathrm{J}_0(\rho)e^{-iz}\,\mathrm{d}\theta_{obj}, \\
&I_{11} = \int_0^{\theta_{\max}} \sin\theta_{obj}\sqrt{\cos\theta_{obj}}\left(t_p^{aSIL}\Phi^{(1)}\sin\theta_{aSIL}\right)\mathrm{J}_1(\rho)e^{-iz}\cos\varphi\,\mathrm{d}\theta_{obj}, \\
&I_{12} = \int_0^{\theta_{\max}} \sin\theta_{obj}\sqrt{\cos\theta_{obj}}\left(t_p^{aSIL}\Phi^{(1)}\sin\theta_{aSIL}\right)\mathrm{J}_1(\rho)e^{-iz}\sin\varphi\,\mathrm{d}\theta_{obj}, \\
&I_{21} = \int_0^{\theta_{\max}} \sin\theta_{obj}\sqrt{\cos\theta_{obj}}\left(t_s^{aSIL}\Phi^{(3)} - t_p^{aSIL}\Phi^{(2)}\cos\theta_{aSIL}\right)\mathrm{J}_2(\rho)e^{-iz}\cos 2\varphi\,\mathrm{d}\theta_{obj}, \\
&I_{22} = \int_0^{\theta_{\max}} \sin\theta_{obj}\sqrt{\cos\theta_{obj}}\left(t_s^{aSIL}\Phi^{(3)} - t_p^{aSIL}\Phi^{(2)}\cos\theta_{aSIL}\right)\mathrm{J}_2(\rho)e^{-iz}\sin 2\varphi\,\mathrm{d}\theta_{obj}
\end{aligned}
\tag{5}
$$

where

$$
\begin{aligned}
&\rho = \sqrt{x^2+y^2};\ \varphi = \tan^{-1}(y/x) \\
&x = -\left(k_{\det}\sin\theta_{\det} x_{\det} + k_{aSIL}\sin\theta_{aSIL} x_d\right) \\
&y = -\left(k_{\det}\sin\theta_{\det} y_{\det} + k_{aSIL}\sin\theta_{aSIL} y_d\right) \\
&z = d(k_{zins} - k_{zaSIL}) - \left(k_{\det}\cos\theta_{\det} z_{\det} + k_{ins}\sqrt{1-\left(\frac{k_{aSIL}}{k_{ins}}\right)^2\sin^2\theta_{aSIL}}\ z_d\right)
\end{aligned}
\tag{6}
$$

The derivation steps between Eqs. (4) and (5) are skipped for the sake of brevity; and these details can be found in Ref [16]. In Eqs. (5) and (6), $k_{\det}$ is the wave number in the detector space. f_{det} is the focal length of the tube lens ($f_{det} >> f_{obj}$), n_{det} is the refractive index of the detector medium, $r_{det} = (x_{det}, y_{det}, z_{det})$ is the location on the detector plane. J(ρ) refers to the Bessel functions of a given order. The relationship between the polar angles, θ_{aSIL}, θ_{obj} and $\theta_{\det}$, is as follows:

$$
\begin{aligned}
n_{obj}\sin\theta_{aSIL} &= n_{aSIL}\sin\theta_{obj} \\
f_{\det}\sin\theta_{\det} &= f_{obj}\sin\theta_{obj} \\
n_{ins}\sin\theta_{ins} &= n_{aSIL}\sin\theta_{aSIL}
\end{aligned}
\tag{7}
$$

The Green's function expressed in the cylindrical coordinates of the detector in Eq. (5). allows us to obtain the far-field image of an arbitrarily oriented dipole located in the proximity of the aplanatic point of the aSIL near the planar interface. Note that the formulation of the Green's function is valid provided that the radius of the aSIL is much greater than the wavelength of light and the distance of the dipole location from the aplanatic location ($R_{aSIL} >> \lambda_0$ and $R_{aSIL} >> |\vec{\mathrm{r}}_{\mathrm{d}}|$) [16], typically satisfied in most practical applications [5–7, 22, 24–26]. A more sophisticated numerical model is required for cases in which such assumption is not valid [27, 28]. The objective and the tube lenses are assumed to be ideal meaning that they are free of optical aberrations and have a transmittance of unity in accordance with the previous studies [14–16]. Such practical details can be incorporated into the model provided that the empirical data is available. Furthermore, the developed electromagnetic model is intended to solve the light propagation from object space to the detector. The stray light originating from the reflections from lens surfaces or chip package are not considered in the image formation process in accordance with the previous studies [3–7, 14–16].

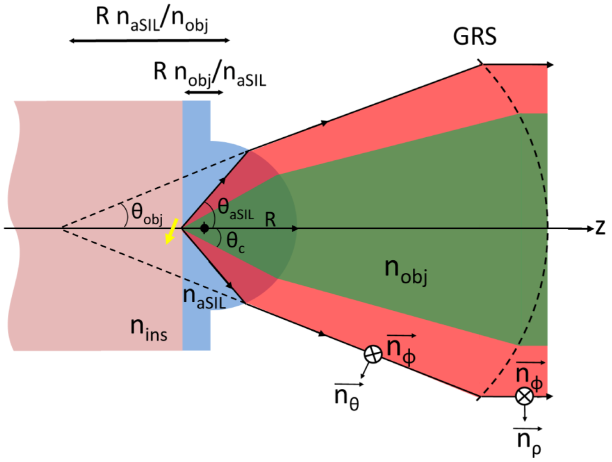

Fig. 1. Schematic of the problem. GRS and R stand for Gaussian reference sphere of the objective and radius of the aSIL, respectively. Green and red zones denote the allowed and forbidden light regions, respectively.

3. Results and discussion

In the following, we first elucidate the characteristics of the forbidden light through studying the field amplitude and phase profile on the objective pupil. Secondly, we investigate the point spread functions to understand the dependence of spatial resolution and light collection efficiency on the depth of the objects. A case of two non-interacting-dipoles is briefly discussed to include the effect of coherence in the spatial resolution. Finally, we discuss the simulated image of two-dimensional objects buried in the insulating medium such as the metal wiring in IC chips.

Following parameters are used in all simulations: $n_{aSIL} = 3.5$, $n_{ins} = 1.53$, $n_{obj} = 1$, $f_{obj} = 10\text{mm}$, $R_{aSIL} = 2.35\text{mm}$, the free space wavelength $\lambda_0 = 1340\text{nm}$ and objective numerical aperture $NA_{obj} = 0.278$. These values reflect typical experimental parameters. The objects are situated on the same transverse plane of aplanatic point of the aSIL ($z_d = 0$), regardless of the their axial distance from the dielectric interface unless it is stated otherwise.

3.1. Field amplitude and phase on the pupil plane

We start by establishing a relationship between the angular distribution of the field derived in Eq. (1) and a geometric ray interpretation to demonstrate the distinct characteristics of subcritical and supercritical angular components of the collected light. Each angular spectrum component is associated with a light ray traveling perpendicular to the phase front of the plane-wave in the silicon immersion medium [16, 29]. Figure 2 shows the intensity profile across the pupil plane ($D_p = 2 f_{obj} NA_{obj} = 5.56\text{mm}$ where D_p refers to the pupil diameter) for axial dipole locations of $d = 0$, $d = \lambda_{ins}/2$ and $d = \lambda_{ins}$ shown left to right. The intensity profile depends strongly on the axial location for both vertical and horizontal dipoles in the forbidden light zone (outside the black circle) unlike the allowed light zone (inside the black circle)

[30]. The longitudinal component of the wave-vector in the insulating medium (k_{zins}) acquires imaginary values at supercritical angles ($\theta_{aSIL} > \sin^{-1}\left(n_{ins} / n_{Si}\right)$) and therefore the amplitude of the supercritical plane wave components in the immersion medium decays rapidly as a function of polar angle θ_{obj} (see Figs. 2(d) and 2(e)).

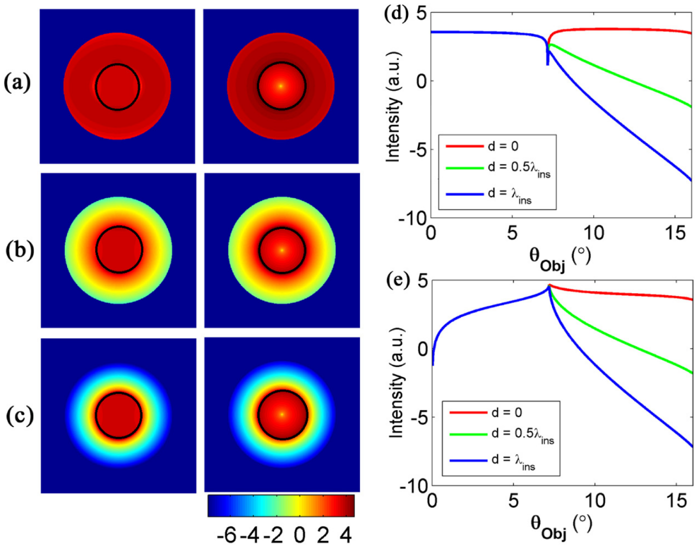

Fig. 2. The logarithm of the electric field intensity map (ignoring the constant $\omega^2\mu_0$) is shown for horizontal dipole (left column) and vertical dipole (middle column) when d = 0 (a), d = $\lambda_{ins}/2$ (b), d = λ_{ins}. The black rings inside the images denote the circle corresponding to the critical angle. The region inside and outside of the ring corresponds to the allowed and forbidden light zones, respectively. The size of each image is 8 mm by 8 mm. (d) A cross section of the intensity profile as a function of polar angle (θ_{obj}) at φ = 0 for horizontal dipole. (e) The same as in (d) except for vertical dipole.

The evanescent wave origin of the propagating waves at the supercritical angles impacts the phase front of the collected light. The phase of a pencil of light at a given polar angle at the pupil is defined: $\vec{\Psi}_{\text{pupil}}(\theta) = \tan^{-1}\left(\text{Im}\left(\vec{\text{E}}^{GRS}\right) / \text{Re}\left(\vec{\text{E}}^{GRS}\right)\right)$. The wave-front aberration originated from the forbidden light is found by subtracting the spherical aberration term $\vec{\Psi}_{\text{sph}} = e^{-i\,k_{zaSIL}\,d}$ from the total phase: $\vec{\Psi}_{\text{FL}} = \vec{\Psi}_{\text{pupil}} - \vec{\Psi}_{\text{sph}}$ [31, 32]. For an aberration-free optical system, $\vec{\Psi}_{\text{pupil}}$ is expected to be a constant and thus independent of the polar angle. Figure 3 plots $\vec{\Psi}_{\text{FL}}$ as a function of polar angle greater than the critical angle of TIR on the Gaussian reference sphere (θ_{obj}) and dipole distance from the dielectric interface *(d)*. Even if the imaging system is free of optical aberrations, collection of evanescent waves introduces ~λ_{ins}/5 peak-to-valley wave-front distortion at high aperture angles, degrading the system performance. Such phase distortion at supercritical angles originates from the complex valued Fresnel transmission coefficients, a condition similarly observed in Goos-Hänchen effect that explains the relative phase shift of a beam undergoing TIR [33]. Note that $\vec{\Psi}_{\text{FL}}$ is independent of the dipole height as the phase distortion originates from the complex Fresnel coefficients (t_s^{ins} and t_p^{ins}) in $\mathbf{\Phi}$ terms in Eq. (3). Furthermore, the phase discontinuity in $\mathbf{\Phi}^{(2)}$ term at the critical angle leads $\text{E}_{\phi}^{\text{GRS}}$ component of the horizontal dipole to have an abrupt π/2 phase shift.

#204581 - $15.00 USD Received 27 Jan 2014; revised 10 Mar 2014; accepted 11 Mar 2014; published 24 Mar 2014

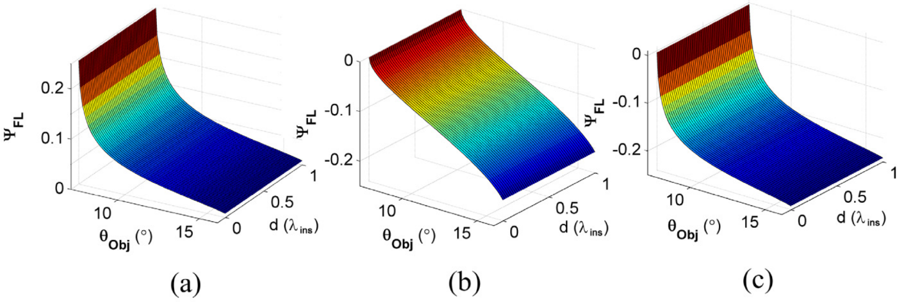

Fig. 3. Wave-front aberration introduced by the forbidden light (Ψ_{FL} in units of radian) in (a) E_{θ}^{GRS} , (b) E_{ϕ}^{GRS} of horizontal dipole and (c) E_{θ}^{GRS} of the vertical dipole as a function of polar angle θ_{obj} and the distance *d* in units of waves. Note that vertical dipole does not have the E_{ϕ}^{GRS} component.

3.2. Image of dipoles on the detector

We study the optical images of dipolar objects on a wide-field detector using the formalism developed in Theory section. The first row in Fig. 4 shows images of a horizontal dipole located on the interface when all light in subcritical and supercritical angles is collected (a), only allowed light is collected (b) and only forbidden light is collected (c). The peak intensity on the detector originating from the forbidden light is approximately an order of magnitude greater as compared to the allowed light. The overall response in (a) is thus dominated by the forbidden light leading to a spot size of approximately $\lambda_{ins}/4$. For a horizontal dipole located at a distance of $d = \lambda_{ins}$ from the interface, the peak intensity of the image originating from the forbidden light is approximately two orders of magnitude smaller as compared to the allowed light as shown in the second row in Fig. 4. The drop in the collected forbidden light in the supercritical aperture angles (compare Figs. 2(a) and 2(c)) as well as the spherical aberration leads to reduction in image brightness and spot confinement even if the dipole is in the geometric focus at the aplanatic point.

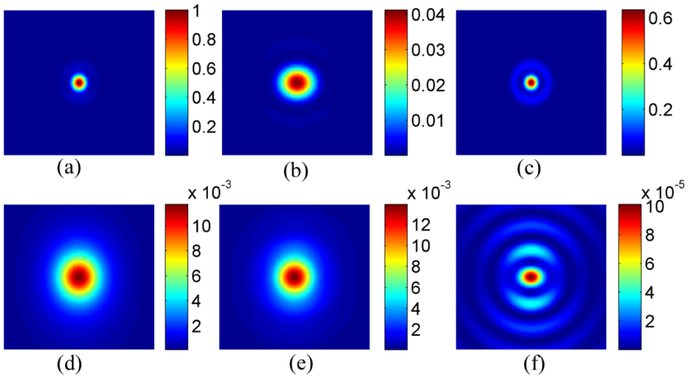

Fig. 4. Normalized wide-field detector images of a horizontal dipole when $d = 0$ (top row) and $d = \lambda_{ins}$ (bottom row). Intensity images for: (a) and (d) full collection NA of the microscope, (b) and (e) only subcritical angle components (allowed light), (c) and (f) only supercritical angle components (forbidden light). The edge length of each image is $3\lambda_{ins}$ x magnification. The color scales are normalized to the maximum intensity in (a).

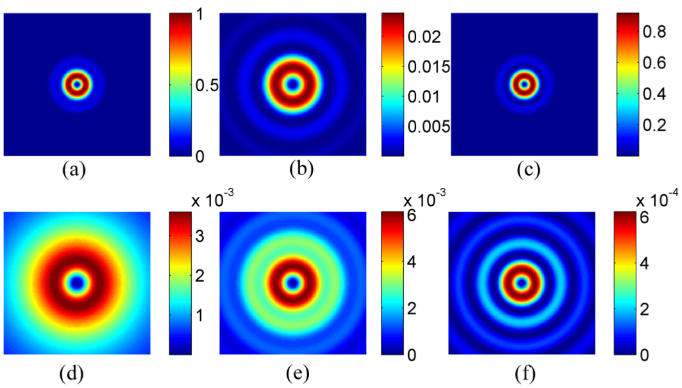

(a) (b) (c)

(d) (e) (f)

Fig. 5. Same as in Fig. 4 except for a vertical dipole.

We repeat the simulations for a vertical dipole and the results are shown in Fig. 5. The vertical dipole images similarly follow the conclusions obtained for horizontal dipole regarding the effect of the forbidden light. When the vertical dipole is located at the interface, the contribution from the forbidden light dominates the overall image and thus leads to a confined spot geometry. At a distance of $d = \lambda_{ins}$, the spot enlarges significantly as the contribution of forbidden light becomes negligible compared to the allowed light.

Figure 6 plots the spot size and relative collection efficiency as a function of dipole height. The intensity image of the dipole is integrated on the detector to calculate the metric of relative collection efficiency and the spot size is defined as the full-width-at-half-maximum of the peak and the dip for the horizontal and vertical dipoles, respectively. The collection of the forbidden light at supercritical aperture angles leads to a spot size as small as $0.2\lambda_{ins}$ and $0.18\lambda_{ins}$ for horizontal and vertical dipoles, respectively. The contribution of the forbidden light becomes negligible with respect to the allowed light when the dipole height reaches $\sim 0.5\lambda_{\text{ins}}$ leading to approximately a factor of 5 drop in collection efficiency as well as loss of the sub-diffraction spatial resolution. Note that the circular symmetry of the spot depends on the distance of the horizontal dipole from the interface unlike the vertical dipole. The circular symmetry of the spot on the detector is preserved for dipole height smaller than $\sim 0.5\lambda_{ins}$, it however transforms into an elliptical spot for larger values of dipole height.

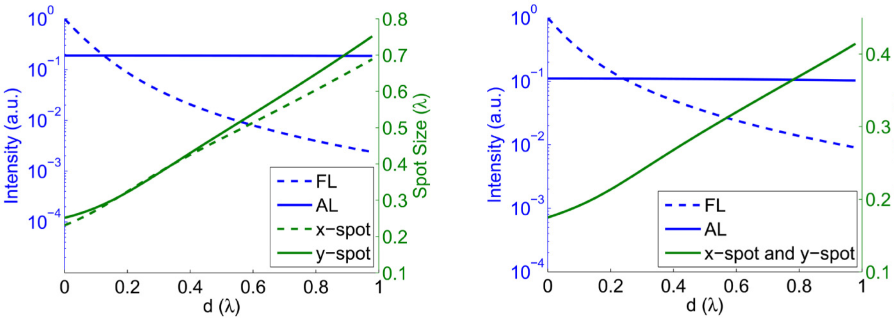

Fig. 6. Collection efficiency shown in intensity axis and spot size (in x and y axes) as a function of dipole height d for horizontal (left) and vertical (right) dipoles. In the vertical dipole case, the spot geometry is circularly symmetric therefore the lines showing the spot size in x and y axes overlap. λ refers to the wavelength in insulating material. FL and AL refer to forbidden light and allowed light.

Two-point resolution refers to the ability of an optical system to resolve two adjacent objects [34]. Such optical analysis is practically important for fault localization through distinguishing the defective feature from a neighboring one in IC failure analysis applications. Figure 7 shows the images of two non-interacting horizontal dipoles separated by a distance of $0.35\lambda_{ins}$ in the limiting cases of complete coherent (in-phase) and incoherent dipoles. According to the Sparrow Criterion, the dipolar objects are resolved both in coherent and incoherent cases when they are both located on the dielectric interface (d = 0) as shown in Fig. 7(a) [35]. A particularly interesting case is when one of the dipole is located at a different depth than the other dipole. Figure 7(b) illustrates this condition when the dipole on the left is located at d = 87.5nm ($0.1\lambda_{ins}$) (typical separation between adjacent interconnect levels) below the right dipole situated on the interface. The reduction in the forbidden light collected from the left dipole renders the peaks no longer resolved in the coherent case. Despite the loss of the modulation depth, the resolution is retained in the incoherent condition and the dip between the two peaks shifted towards the dipole on the left [36]. When both dipoles are situated at d = 87nm ($0.1\lambda_{ins}$), they become completely unresolved in the coherent case and the modulation depth between the peaks of the incoherent dipoles is reduced by ~30%.

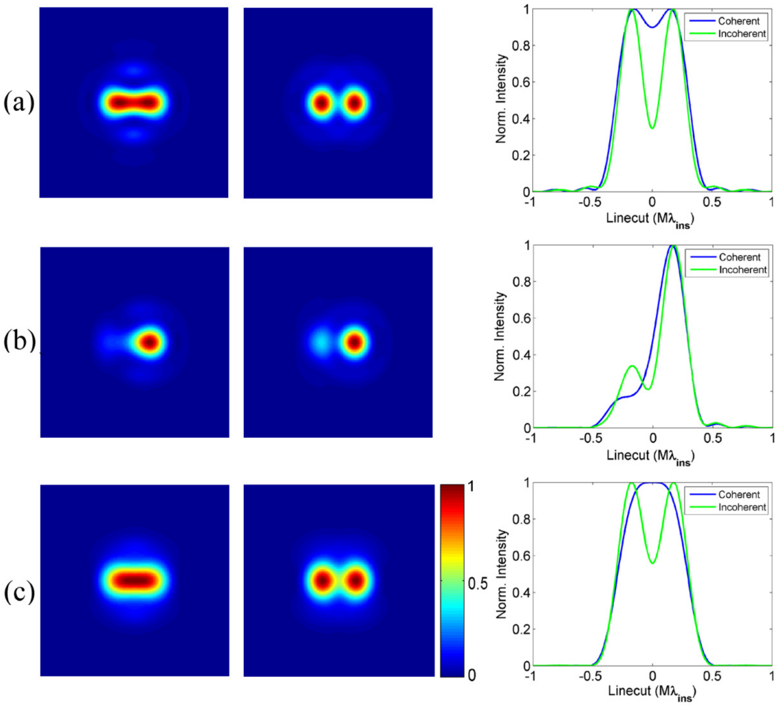

Fig. 7. Normalized wide-field detector images of two dipoles separated by $0.35\lambda_{ins}$ when (a) both dipoles positioned at d = 0, (b) dipole on the right at d = 0 and the dipole on the left at d = $0.1\lambda_{ins}$. First column corresponds to coherent case, middle column corresponds to incoherent case and the third column is for the cross sections of the two conditions along the lateral axis. The edge length of each image is $2\lambda_{ins}$ x magnification.

3.3. Image of two dimensional objects on the detector

We simulate incoherent wide-field images of two-dimensional objects buried in the insulating medium to study the imaging performance on test objects encountered in IC chips. We assume the horizontally polarized incoherent illumination is uniform in the field of view and the optical system has the configuration explained at the beginning of the section.

A typical test object for the optical analysis is critical dimension features for estimating the spatial resolution and contrast at various interconnect levels. Figure 8 shows the optical image of such a test structure located at an axial distance of d = 0, 438nm ($0.5\lambda_{ins}$) and 876nm (λ_{ins}) from the dielectric interface, from left to right, respectively. The line pitch ranges from 175nm ($0.2\lambda_{ins}$) to 700nm ($0.8\lambda_{ins}$) with an increment of 87.5nm ($0.1\lambda_{ins}$) between each group. All groups except the first one are well resolved according to Sparrow criterion in d = 0 case.

The smallest groups resolved in the latter cases are the fourth and the seventh groups, respectively. Note that the difference of image brightness between Figs. 8(a) and 8(b) is more drastic as compared to the difference between Figs. 8(b) and 8(c) due to the exponential decay of the forbidden light intensity as a function of the object distance from the interface.

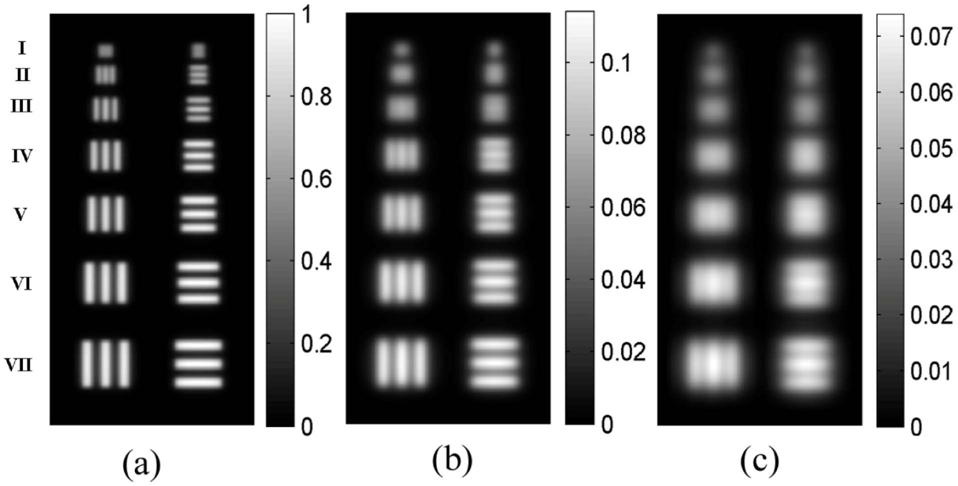

Fig. 8. Simulated images of a resolution target with periodic grating structures at different depth with respect to the dielectric interface. (a) $d = 0$, (b) $d = 438\text{nm}$ ($\lambda_{ins}/2$), (c) $d = 876\text{nm}$ (λ_{ins}). The size of each image is 7.32μm x 15.52μm (8.3λ_{ins} x 17.7λ_{ins}) x magnification.

In practice, closely spaced objects are typically found at different interconnect levels in ICs. Figure 9(a) illustrates an example of metal wiring with a constant line pitch of 876nm (λ_{ins}) in the transverse plane and located at $d = 438\text{nm}$ ($\lambda_{ins}/2$) and $d = 876\text{nm}$ (λ_{ins}), shown in red and blue colors, respectively. Figure 9(b) shows the simulated optical image of the metal wiring assuming the aplanatic plane coincides with the plane of L1 and L2. According to the vertical linecut obtained from the optical image, L1 and L2 are well resolved according to Sparrow's criterion at which the valley between the peaks reaching down to ~0.45 whereas the modulation contrast between the peaks of L3 and L4 is almost vanishing (~0.02). The slight difference in the intensity level of the dip between L2-L3 and L3-L4 peaks originates from the unequal contrast level of the L2 wire with respect to L3 and L4, as explained in the two-point resolution case study.

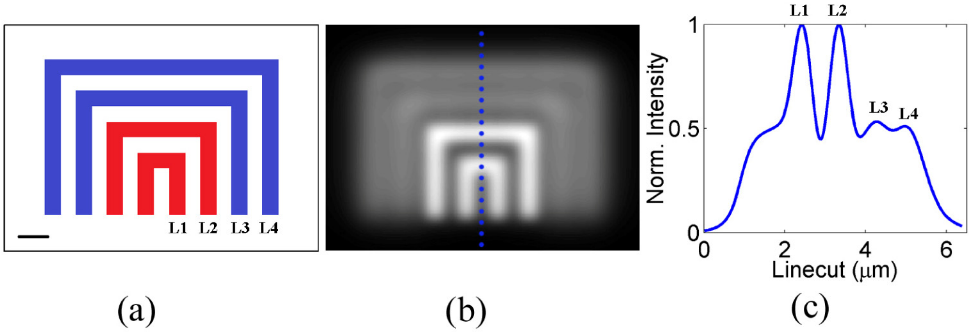

Fig. 9. Layout and the simulated images of a buried two-level metal wiring. (a) The red and blue lines are located at a distance of $\lambda_{ins}/2$ and λ_{ins}, respectively. The scalebar corresponds to a length of 876 nm (λ_{ins}). (b) The optical image of the object. (c) Cross section of the image along the dotted line shown in (b). The size of the images corresponds to a field of view of 8.86μm x 6.38μm (10.11λ_{ins} x 7.28λ_{ins}) x magnification.

#204581 - $15.00 USD Received 27 Jan 2014; revised 10 Mar 2014; accepted 11 Mar 2014; published 24 Mar 2014

The examples above are chosen considering the dielectric structure of the conventional bulk silicon process technology in which the interconnect layers are buried beyond a single dielectric interface between the silicon substrate and the insulating media. Our model can be also applied to more complex layered media applications such as silicon-on-insulator chips in which the silicon junction is contained between a thin buried insulating box and the insulating media surrounding the interconnect layers. In order to account for the multiple reflections occurring in the stratified media, the generalized Fresnel coefficients can be used in place of the Fresnel coefficients used here [37]. Besides the concerns originating from the evanescent modes, practical complications further affect system performance such as the optical aberrations originating from imperfect solid immersion lens dimensions, spectral bandwidth of the light and the change in the operating temperature of the chips. Such practical issues will be investigated in future through adapting the Green's function model developed in this study.

4. Conclusion

In this theoretical study of forbidden light in high NA aSIL microscopy, we demonstrated that the dielectric interface between the silicon substrate and insulating medium surrounding the circuit features has a major impact on the imaging performance. Circuit features located within a half-wavelength of the interface, comprising the gate and first few metal levels of the modern IC chips, can be interrogated effectively with sub-diffraction transverse spatial resolution and high photon collection efficiency due to the forbidden light collected by the aSIL microscope. For objects buried farther into the insulating medium, only light from the allowed light zone can be collected, leading to up to a factor of 5 drop in light collection efficiency. In addition, the diffraction limited spatial resolution is compromised due to optical aberrations imposed by the dielectric interface.

The developed vector field theory for evaluating the effects of evanescent waves in aSIL microscopy of ICs can assist in quantitative analysis of optical images in the context of fault isolation and failure analysis as well as designing adaptive optics for compensating optical aberrations for high resolution optical inspection as pure ray-tracing model based software cannot account for the behavior of the evanescent waves. Even though the focus of this study is limited to semiconductor IC applications in which the resonant scattering is usually of interest, the model can be adapted to applications in fields such as quantum optics and biophotonics for which the non-resonant scattering processes are also important.

Acknowledgment

This work was supported by Intelligence Advance Research Programs Activity via Air Force Research Labs under contact no: FA8650-11-C-7102. Bennett. B. Goldberg and M. Selim Ünlü are co-corresponding authors